Int. J. Electrochem. Sci., 14 **(2019)** 11138 – 11151, doi: 10.20964/2019.12.83

International Journal of ELECTROCHEMICAL SCIENCE
www.electrochemsci.org

Surface Characteristics and Electrochemical Performance of Activated Carbons from *Schinus molle* Stones Prepared by Hydrothermal Carbonization and KOH Activation

Carlos Moreno-Castilla[*]*, Helena García-Rosero, Francisco Carrasco-Marín.*

Departamento de Química Inorgánica, Facultad de Ciencias, Universidad de Granada, 18071 Granada, Spain.
[*]E-mail: cmoreno@ugr.es

Received: 20 February 2019 / *Accepted:* 30 March 2019 / *Published:* 29 October 2019

Schinus molle (SM) stones contain *ca*. 47 % C and 1 % N and are therefore a potential raw material for the preparation of activated carbons (ACs) with N functionalities. In this study, we investigated the usefulness of SM stones to prepare ACs by hydrothermal carbonization (HTC) followed by KOH activation. For comparison purposes, ACs were also prepared by direct KOH activation of pristine SM stones. The objective was to study the effects of each preparation method on the physico-chemical surface and electrochemical performance of the ACs obtained. Ash content was lower and N content higher in ACs produced by HTC-KOH activation (HSM series) *versus* direct KOH activation (SM series). All ACs, except the most highly activated sample from the HSM series, had narrow micropores or constricted micropore entrances. The highest surface area and mesopore volume obtained were 1464 m^2 g^{-1} and 0.29 cm^3 g^{-1}, respectively. Examination of AC porosity and surface area indicated that SM stones were more reactive to KOH activation after HTC. AC HSM200-2 had the largest capacitance, 235 F g^{-1} at 0.5 A g^{-1}, and the highest energy density, 7.83 Wh kg^{-1}, at a power density of 400 W kg^{-1}. The electrochemical performance of this sample was comparable to that recently reported for a wide variety of biomass-based ACs.

Keywords: Activated carbons; Schinus molle stones; Hydrothermal carbonization; Surface characteristics; Electrochemical performance.

1. INTRODUCTION

Activated carbons (ACs) are porous materials with a well-developed porosity, high surface area, versatile surface chemistry, and good physicochemical stability. These characteristics make them useful for multiple applications in: water remediation; gas separation, purification, and storage; catalysis; and energy storage [1-6]. ACs have long been produced from lignocellulosic biomass residues [1-3] but have

recently attracted renewed interest in relation to novel applications in energy storage and water remediation [7-10].

ACs are classically prepared by physical or chemical activation of the pristine or carbonized raw material, most frequently by KOH chemical activation [11]. Nowadays, HTC of lignocellulosic biomass and carbohydrates is also used to prepare ACs and carbon materials with different functions [8,12-17], heating an aqueous solution or dispersion of the raw material in an autoclave at temperatures below 250 ºC. This process, although not novel, is simple, low-cost, and low-energy, and it is considered a "green" synthetic procedure [12,13,18,19]. The hydrochar obtained contains different functionalities but does not generally have an open porosity, one of the main drawbacks of HTC materials produced directly from carbohydrates or biomass. For this reason, they require activation before they can be applied for adsorption, catalysis, or energy storage [19,20].

SM is a widely planted ornamental tree in many Mediterranean countries. SM stones are sphere-like and around 3-4 mm in diameter. Elemental analysis of the biomass precursor is usually applied to determine its viability to produce carbon materials. SM stones have a carbon content of *ca*. 47 wt% (*vide infra*), which is adequate for their utilization as raw material for ACs [12]. They also possess a nitrogen content of *ca*. 1 wt% (*vide infra*), potentially allowing the preparation of ACs with different nitrogen functionalities that are important in some adsorption, catalysis, and energy storage processes [21-24].

The aim of this study was to evaluate the usefulness of SM stones as raw material to prepare ACs for application as supercapacitor electrodes in energy storage [6,7,10]. ACs were prepared by HTC at between 150 and 200 ºC followed by KOH activation or, for comparison purposes, by direct KOH activation of the pristine raw material. The objective was to determine the effects of the preparation method on the morphology, surface chemistry, pore texture, and electrochemical performance of both series of ACs.

2. EXPERIMENTAL

2.1. Preparation of activated carbons

Stones were obtained from the SM fruit by removing the peel, pulp, and stalk and were dried at 110 ºC. They were then hydrothermally treated at between 100 and 200 ºC for 1 h after placing a mixture of 50 g dried SM stones and 100 mL distilled water in a 250 mL Teflon-lined autoclave. The resulting hydrochars are henceforth designated as HSMt, with t being the treatment temperature. Hydrochars were activated by impregnation with a concentrated KOH solution at a KOH/hydrochar mass ratio of 2 or 4 and by subsequent carbonization at 800 ºC for 1 h in a N_2 flow. The ACs obtained were treated with 1M HCl and then washed with distilled water until chloride ions disappeared from the washing water. These ACs are designated as HSMt-x, with x indicating the KOH/hydrochar mass ratio. The same procedure was followed for the direct KOH activation of dried SM stones, and the resulting ACs are designated as SMx

2.2. Characterization

The morphology of samples was examined using a FEI Quanta 400 environmental scanning electron microscope. Proximate analysis of the SM stones was determined using a Shimadzu TGA-50H thermobalance. The sample was heated at 20 ºC min^{-1} under N_2 flow (100 mL min^{-1}) from room temperature to 120 ºC over 1 h and then heated to 800 ºC to determine the moisture and volatile compound contents. When a constant weight was reached, the N_2 flow was changed to air in order to determine the fixed carbon and ash contents.

C, H, and N contents were determined by elemental analysis using Thermo Finnigan equipment (1112 series). N and O contents were also determined by XPS using an Escalab 200R system (VG Scientific Co.) equipped with MgK_α X-ray source ($h\gamma$ = 1253.6 eV) and hemispherical electron analyzer. The C_{1s} peak at a binding energy (BE) of 284.6 eV was used as internal standard.

N_2 and CO_2 adsorption isotherms were determined at -196 and 0 ºC, respectively, using an Autosorb 1 from Quantachrome. The BET equation was applied to the N_2 adsorption isotherm to obtain the surface area, S_{BET}, and the DR equation was applied to both isotherms to obtain the micropore volume, W, and micropore width, L. The total pore volume, $V_{0.95}$, was obtained from the amount of liquid N_2 adsorbed at p/p_0 = 0.95.

2.3. Electrochemical measurements

Electrochemical measurements were made at room temperature with 1M H_2SO_4 as electrolyte in two- and three-electrode cells, 2EC (Teflon-Swagelock-type) and 3EC, respectively, following the method described elsewhere [25]. Thus, working electrodes were prepared from a well-mixed slurry of the ACs (90 wt.%) with polytetrafluorethylene (PTFE) emulsion (10 wt.%) as binder. The slurry was pressed at 3 bar on graphite paper disks (2EC) or graphite foil (3EC) and dried overnight in an oven at 120 ºC. The discs had an area of *ca*. 0.50 cm^2 (ϕ 8 mm) and contained the same amount of active material, *ca*. 4 mg, while the graphite foil contained *ca*. 20 mg of active material. Electrodes were immersed in the electrolyte for five days before assembly in the cells. The 2EC comprised two identical electrodes separated by a porous fibrous separator impregnated with the electrolyte solution. The 3EC comprised the above slurry pasted on graphite paper as working electrode with a reference electrode (Ag/AgCl) and counter electrode (Pt wire).

Cyclic voltammetry (CV) and galvanostatic charge-discharge (GCD) were carried out using a Biologic VMP-300 potentiostat. CVs and GCDs were performed in the 0-0.85 V range at a scan rate of 2.5 mV s^{-1} for CVs and current densities between 0.14 and 5 A g^{-1} for GCDs.

Gravimetric capacitance, C (F/g), was obtained from the discharge curves of the GCDs by equation (1):

$$C = I_d \Delta t / m \Delta V \qquad (1)$$

where I_d is the discharge current, Δt the discharge time, m the total mass of the AC in the electrodes, and ΔV the voltage interval after the ohmic drop. The coulombic efficiency was calculated from the discharge and charge time, t_d and t_c, respectively, using the formula $(t_d/t_c)100$.

For performance comparisons, the gravimetric capacitances in 2EC obtained from the above equation were multiplied by four to obtain the expression per single electrode, which is the 3EC equivalent [26]. However, *per convention*, the gravimetric capacitances obtained from equation (1) in 2EC, C_{2EC}, were used to calculate the energy density in the Ragone plot using the equation $E = C_{2EC}(\Delta V_d)^2/2$, where ΔV_d is the operation voltage taken as $\Delta V_d = V_{max} - IR_{drop}$. Power density was calculated from $P = E/\Delta t$ [27,28].

3. RESULTS AND DISCUSSION

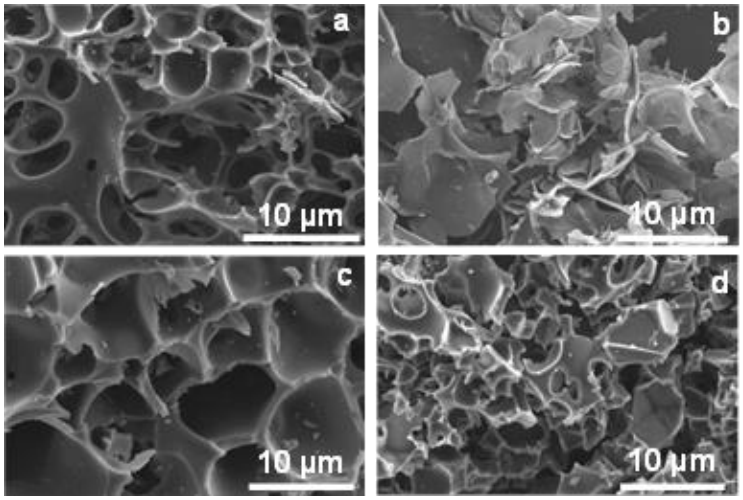

Figure 1. Environmental scanning electron microscopy images of activated carbons: (a) HSM150-2, (b) HSM150-4, (c) SM2 and (d) SM4.

Table 1. Ash content (%), elemental analysis (%) in dry-ash-free basis, and nitrogen and oxygen contents (wt%) by XPS of precursor, hydrochars, and activated carbons

Sample	Ash	C	H	N	O*	N_{XPS}	O_{XPS}
SM	6.28	46.95	6.57	0.98	45.50	nd	nd
HSM100	5.90	50.82	6.61	1.23	41.34	nd	nd
HSM150	3.98	57.45	6.12	1.34	35.09	nd	nd
HSM200	2.10	63.92	6.10	1.48	28.50	nd	nd
HSM100-2	5.54	76.85	1.05	0.90	21.20	1.1	12.2
HSM150-2	3.63	71.46	1.06	1.31	26.08	1.3	12.0
HSM200-2	2.00	69.24	1.11	1.40	28.25	1.4	11.7
HSM150-4	3.20	82.56	0.71	0.96	15.77	0.9	6.6
SM2	5.63	77.47	0.56	0.62	21.35	0.7	12.0
SM4	5.30	86.78	0.31	0.77	12.14	0.8	11.8

Figure 1 depicts micrographs of selected ACs. Samples HSM150-2 and SM2 had a similar morphology, with very large pores and conchoidal cavities caused by the brittle fracture of precursor particles during KOH activation [25]. The most activated samples, HSM150-4 and SM4, showed a greater degree of fracture of precursor particles during activation, with the disappearance of most of the cavities and larger pores.

Table 1 displays the ash content and elemental analysis of the precursor, hydrochars, and ACs with the XPS results for N and O contents of ACs. Proximate analysis of the precursor in dry basis yielded: volatile compounds 50.10 wt%, ash 6.28 wt%, and fixed carbon 43.62 wt%. Elemental analysis of biomass is usually employed to check its viability as carbon precursor [12], and the high carbon content of SM stones (46.95 wt%) enables their use as raw material to prepare ACs. Moreover, in this case, the raw material also has a high fixed carbon content, which would produce a high yield in the HTC process. Elemental analysis and XPS measurements of N and O can be considered as the total and surface contents, respectively, indicating their distribution in the ACs.

The ash content of the SM stones was reduced by HTC, and the reduction was greater with higher HTC temperature due to solubilization of the inorganic matter of the precursor. Consequently, the ash content was lower in ACs from the HSM *versus* SM series. The N and O content of the precursor was also affected by HTC, which increased total N content and reduced oxygen content, with these changes being greater at higher temperatures.

Table 2. Binding energy (eV) and area (%) of N_{1s} and O_{1s} peaks from XPS patterns of activated carbons

Sample	N_{1s} BE (peak area)	O_{1s} BE (peak area)
HSM100-2	398.2(26), 400.0(47), 401.0(26)	531.6(21), 533.0(79)
HSM150-2	398.4(12), 400.1(78), 401.3(11)	531.4(39), 533.0(61)
HSM200-2	398.4(14), 400.0(67), 401.3(19)	531.4(28), 532.9(72)
HSM150-4	398.7(16), 400.2(72), 401.5 12)	531.7(41), 533.1(59)
SM2	398.2(28), 400.1(47), 401.0(18), 402.4(7)	531.6(36), 533.0(64)
SM4	398.2(29), 400.0(48), 401.0(17), 402.8(7)	531.6(36), 533.0(64)

The increase in N content was attributed to Maillard-type reactions between N compounds and carbohydrates in the raw material during HTC [19]. Thus, the N was covalently bonded to the carbon network and remained part of the parent carbon during subsequent heating for activation of the hydrochar [19]. Hence, total N content was higher in the ACs from the HSM series than in those from the SM series. The total O content of the hydrochars decreased at higher HTC temperatures because of the increase in C content.

KOH activation of the hydrochars produced an increase in their C content, which was lower at higher HTC temperatures, and a decrease in their ash and total N and O contents. The increase in KOH/precursor mass ratio also produced, in both AC series, a decrease in ash, total N (except in SM4), and O contents. N_{XPS} and total N content were similar in both AC series, whereas the O_{XPS} was lower than the total O content except in SM4.

N_{1s} core level spectra of the ACs are depicted in Figure 2, and the results are compiled in Table 2. All ACs from the HSM series showed three peaks with BE of around 398.4, 400.1, and 401.3 eV.

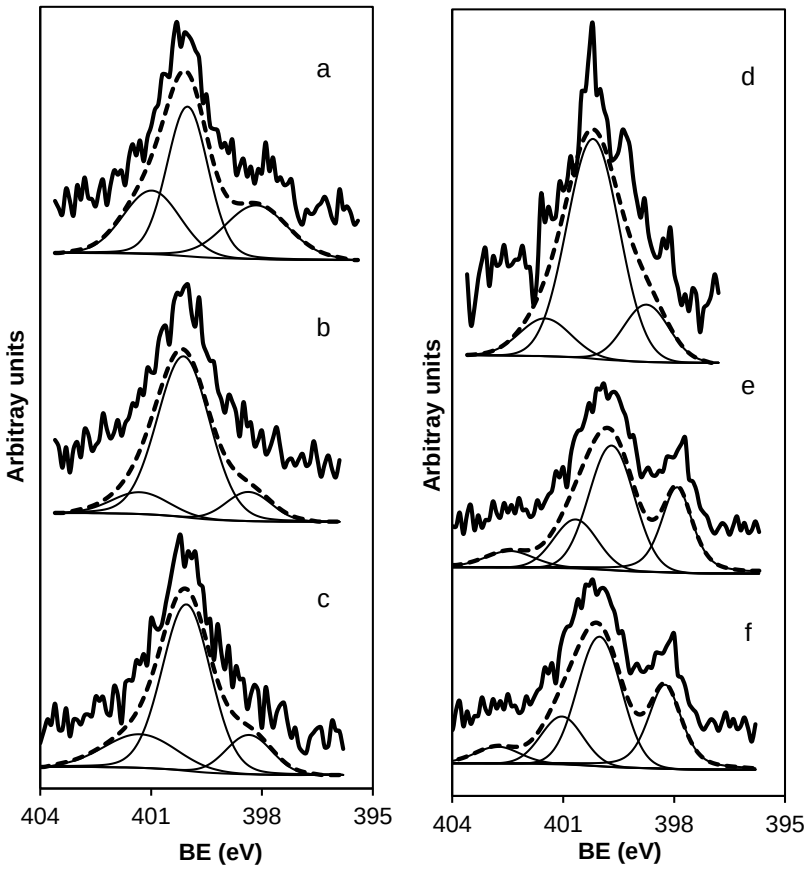

Figure 2. XP spectra of the N_{1s} region of activated carbons: (a) HSM100-2, (b) HSM150-2, (c) HSM200-2, (d) HSM150-4 (e) SM2 and (f) SM4.

The peak at 398.4 eV was due to pyridines, N-6 functionalities [29], and the second peak at 400.1 eV was due to pyrrolic-N or pyridonic-N, N-5 functionalities [30]. The third peak at 401.3 eV can be assigned to N within or in a valley position of a graphene layer, i.e., quaternary-N (N-Q functionalities) [30,31], and the most abundant functionalities were N-5 (47 - 78 %).

ACs from the SM series showed the same three peaks plus a fourth at around 402.6 eV that can be assigned to pyridine-N-oxide (N-X functionalities), i.e., pyridinic N bonded to oxygen species [22,32]. These N-X functionalities are formed when pyridine functionalities on the external surface are exposed to atmospheric air [23]. In this case, the most abundant functionalities were again N-5 (~ 48 %), followed by N-6 (~ 29 %).

O_{1s} core level spectrum (not shown) had two components in all samples, the first at BE between 531.0 and 531.6 eV, assigned to double C=O bonds in ketone, quinone, and carboxyl acid groups, and the second at BE between 532.9 and 533.3 eV, assigned to C–O bonds from alcohols, phenols, and ethers [33,34]. These last functionalities were the most abundant in all cases.

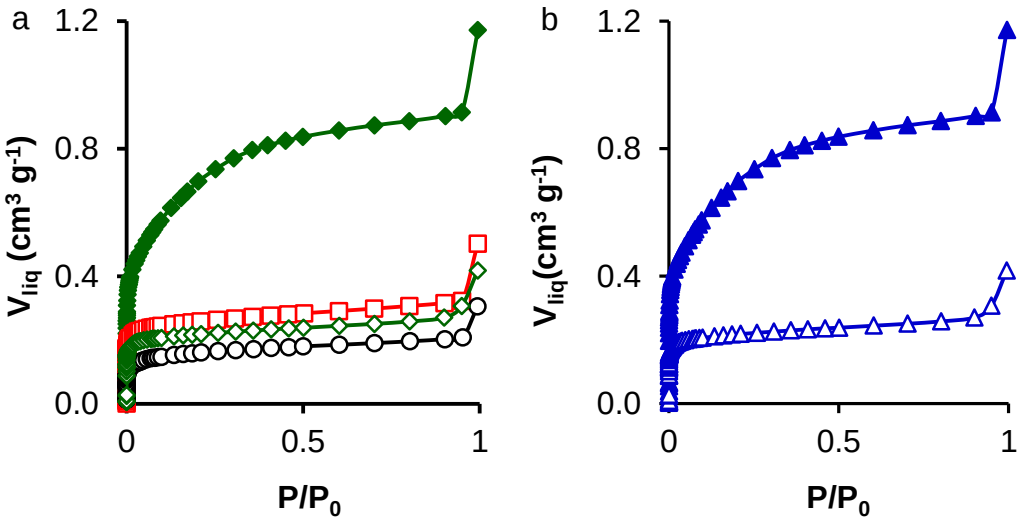

Figure 3. N_2 adsorption isotherms on activated carbons at -196 ºC: a) ○, HSM100-2; ◇, HSM150-2; □, HSM200-2; ◆, HSM150-4. b) △, SM2; ▲, SM4.

Table 3. Porosity and surface area of activated carbons

Sample	W_{N2}	W_{CO2}	W_{N2}/W_{CO2}	L_{N2}	L_{CO2}	$V_{0.95}$	S_{BET}
	cm^3 g^{-1}	cm^3 g^{-1}		nm	nm	cm^3 g^{-1}	m^2 g^{-1}
HSM100-2	0.14	0.32	0.44	1.10	0.71	0.22	382
HSM150-2	0.21	0.35	0.60	0.78	0.74	0.31	532
HSM200-2	0.24	0.33	0.73	0.82	0.78	0.35	627
HSM150-4	0.62	0.43	1.44	1.56	0.78	0.91	1464
SM2	0.14	0.32	0.44	1.44	0.70	0.23	378
SM4	0.27	0.37	0.73	1.26	0.79	0.51	661

N_2 adsorption isotherms of the ACs (Fig. 3) were type I, typical of microporous solids [35], although they also contained some mesopores because of a slight increase in N_2 uptake at high relative pressure after micropore filling. This increase was higher in the most activated samples, HSM150-4 and SM4. In addition, the shape of the isotherm in HSM150-4 showed a wide knee, as in the case of type I(b) isotherms, indicating a wide micropore size distribution and narrow mesopores (below ~ 3nm). Table 3 exhibits the porosity and surface area of ACs obtained from the adsorption isotherms. W_{CO2} was

higher than W_{N2} in all ACs, except in HSM150-4, indicating narrow micropores or constrictions at their entrances that made them less accessible to N_2 molecules at –196 ºC than to CO_2 molecules at 0 ºC [36,37]. The difference between W_{N2} and W_{CO2} decreased (and the W_{N2}/W_{CO2} ratio increased) at higher HTC temperatures and KOH/precursor mass ratios, due to the disappearance of constrictions at micropore entrances and/or to micropore widening. In addition, the W_{N2}/W_{CO2} ratio was higher in ACs from the HSM *versus* SM series for the same KOH/precursor mass ratio.

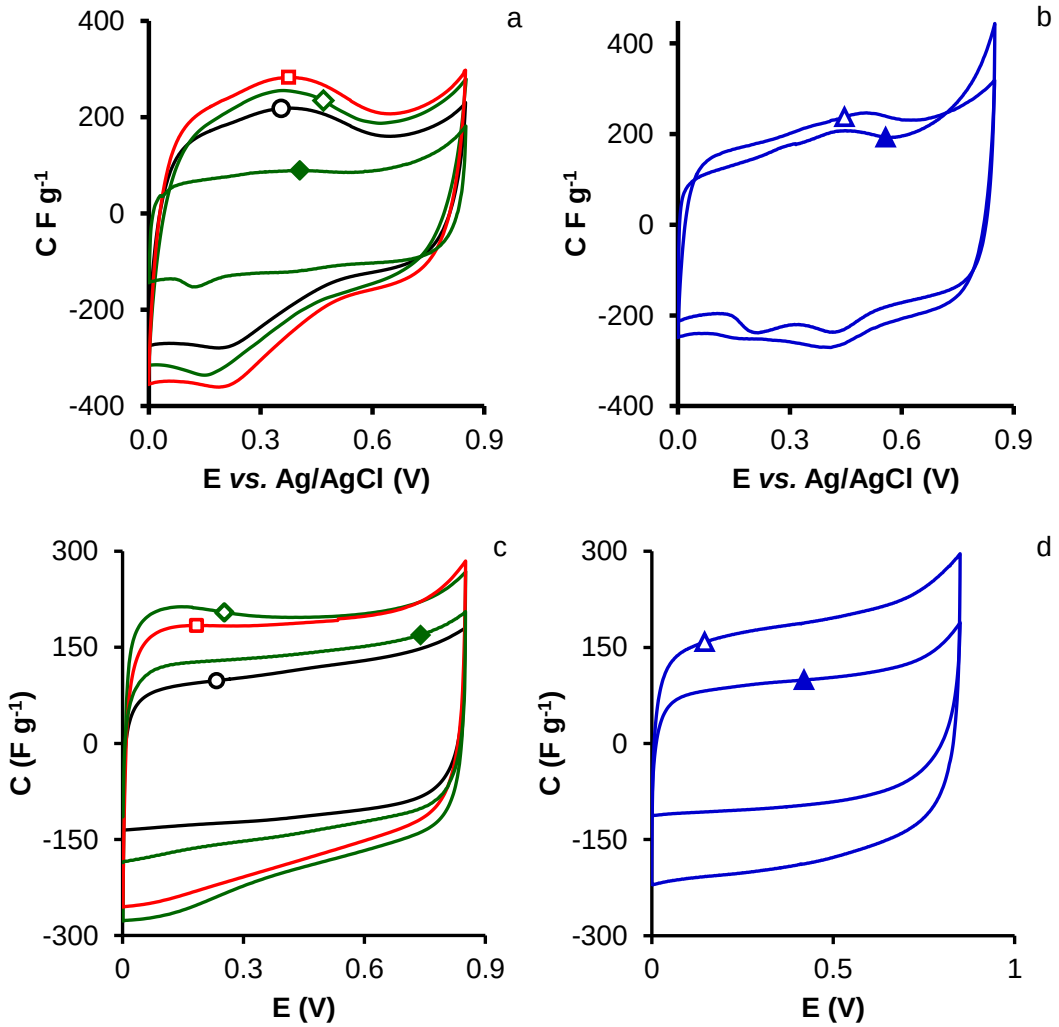

Figure 4. CVs at 2.5 mV s^{-1} in 3EC (a, b) and 2EC (c, d). Samples (a, c): ○, HSM100-2; ◇, HSM150-2; □, HSM200-2; ◆, HSM150-4 and (b, d) △, SM2; ▲, SM4.

Except for the most activated samples, HSM150-4 and SM4, the $V_{0.95}$ value was lower than the W_{CO2} value in all ACs, indicating that not all of their micropores were accessible to N_2 molecules due to diffusional limitations, even at the high relative pressure of 0.95 at – 196 ºC.

HSM100, HSM150, and HSM200 hydrochars exhibited a S_{BET} of 23, 26, and 27 m^2 g^{-1}, respectively, and they therefore required activation to increase their surface area and porosity. The S_{BET} of ACs in the HSM series increased with higher HTC temperature and was higher than S_{BET} values of the SM series for the same KOH/precursor mass ratio. We highlight the very large surface area of

HSM150-4, *ca*. 1500 $m^2 g^{-1}$, with a mesopore volume of 0.29 $cm^3 g^{-1}$ (from $V_{0.95}$– W_{N2}) that represented *ca*. 32 % of the total porosity.

Examination of the porosity and surface area of the ACs indicated that the SM stones were more reactive to KOH activation after HTC, attributable to: i) the complex chemical reactions of SM stone carbohydrates during HTC, leading to incipient carbonization, as shown by the increased C content of the hydrochars (Table 1); and ii) the lower ash content of HSM hydrochars than of SM stones.

Figure 4 depicts CVs at 2.5 mV s^{-1} obtained with 3 and 2EC. CVs obtained with 3EC are very useful for analyzing faradic reactions and voltages at a single surface [38,39], showing a quasi-rectangular shape and a clear faradic hump indicating the presence of pseudocapacitance phenomena, attributed to the O and N functionalities [40] possessed by all of the ACs. However, CVs obtained with 2EC had a rectangular shape with no pseudocapacitance effects.

GCDs at 0.5 A g^{-1} (Fig. 5) showed a triangular shape with a coulombic efficiency of 100 % in all cases. The gravimetric capacitance increased (Table 4) with higher HTC temperature in the HSM series, and the capacitance decreased with higher KOH/precursor mass ratio in both series. These variations in capacitance can be attributed to differences in the surface functionality and porosity of the ACs.

Table 4. Gravimetric capacitance from GCDs at 0.5 A g^{-1}, and capacitance retention and Coulombic efficiency at 5 A g^{-1}. Energy density released at 400 W kg^{-1} (E_{400}).

Sample	C	Retention	Efficiency	E_{400}
	F g^{-1}	%	%	Wh kg^{-1}
HSM100-2	171	38	97	3.03
HSM150-2	227	68	97	4.23
HSM200-2	235	50	99	7.83
HSM150-4	125	60	92	2.62
SM2	183	63	97	4.35
SM4	90	80	91	1.40

Thus, total N and O contents were increased at higher HTC temperatures in the HSM series of ACs. Most of these functionalities are fixed on the micropore walls and cannot be detected by XPS, but they would affect the formation of the double-layer within the micropores, introducing pseudocapacitance effects. This is possible because the micropores of HSM samples were accessible to hydronium ions (0.36-0.42 nm) [41] and hydrated bisulfate ions (0.53 nm) [42]. In addition, W_{N2}, L_{CO2}, and S_{BET} values were increased at higher HTC temperatures in the HSM series of ACs. In contrast, the capacitance was decreased at higher KOH/precursor mass ratios, mainly caused by the opening of the porosity and consequent appearance of mesopores.

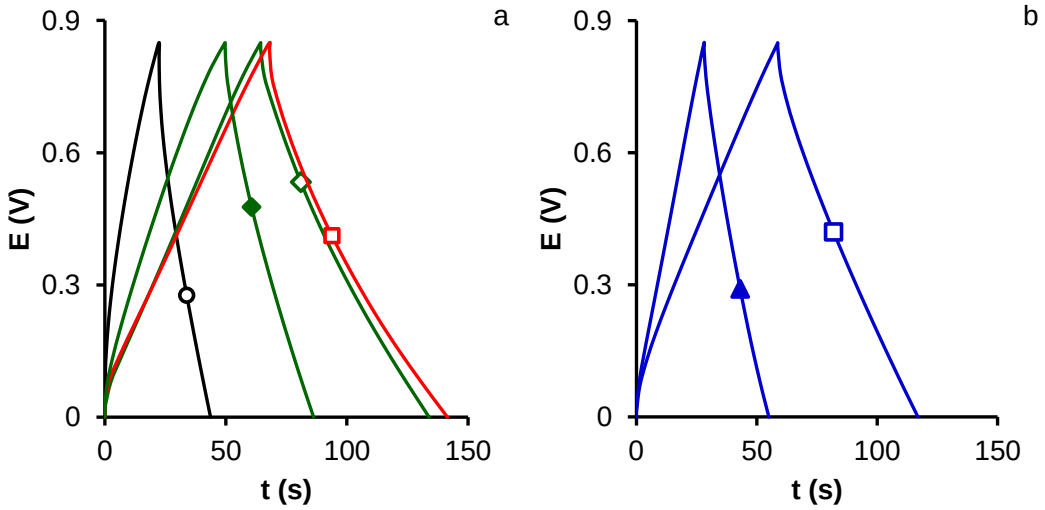

Figure 5. GCDs at 0.5 A g^{-1} in 2EC of samples (a): ○, HSM100-2; ◇, HSM150-2; □, HSM200-2; ◆, HSM150-4 and (b) △, SM2; ▲, SM4.

HSM200-2 showed the highest gravimetric capacitance, 235 F g^{-1}, at 0.5 A g^{-1}, which is comparable with or even higher than that of recently reported biomass-derived ACs (Table 5). The gravimetric capacitance decreased with higher current density (Fig. 6 and Table 4), due to cell resistance. Likewise, the Coulombic efficiency was lower at 5 A g^{-1} than at 0.5 A g^{-1} (Table 4).

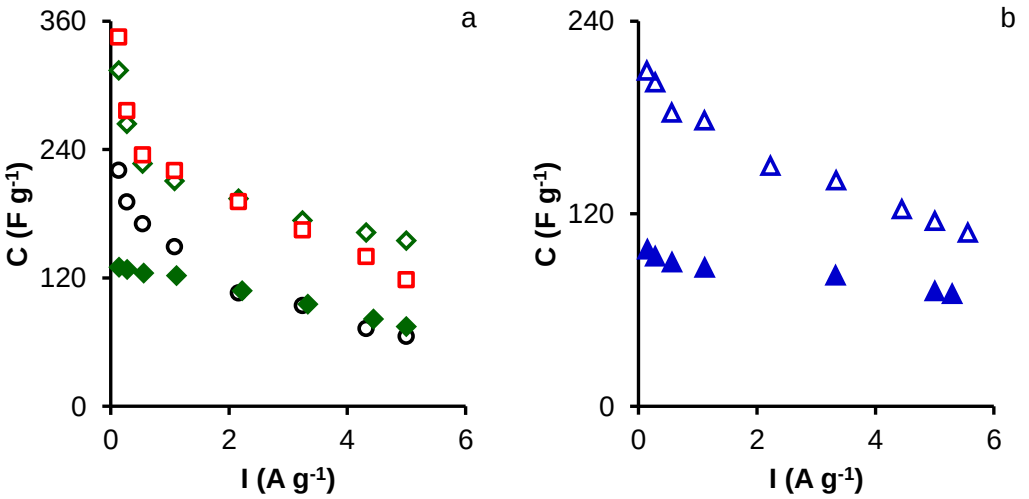

Figure 6. Variation of the gravimetric capacitance with current density of samples (a): ○, HSM100-2; ◇, HSM150-2; □, HSM200-2; ◆, HSM150-4 and (b) △, SM2; ▲, SM4.

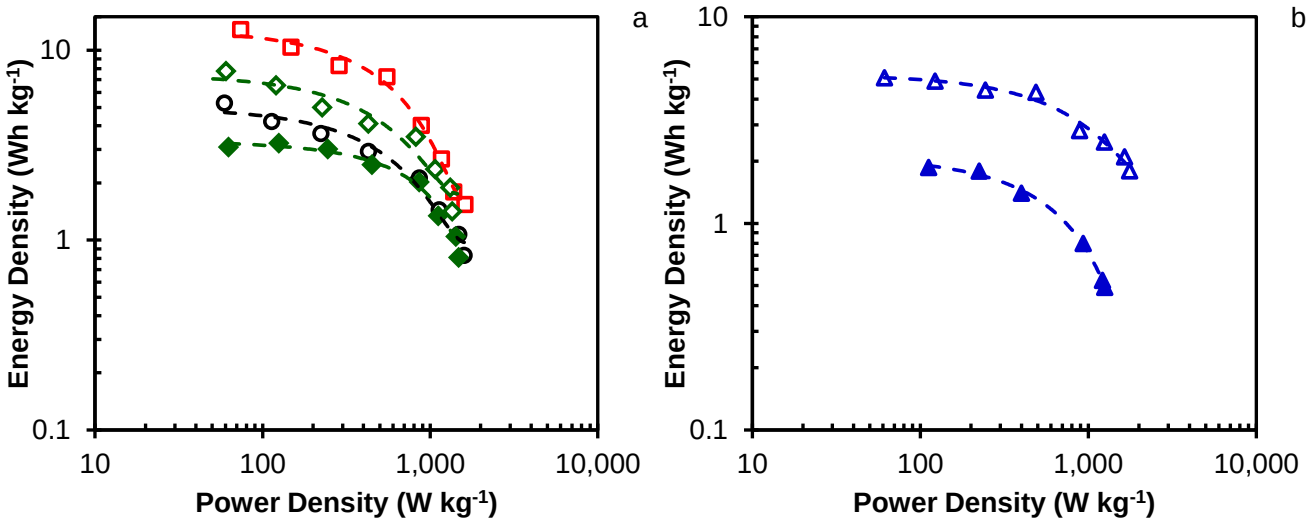

Figure 7. Ragone plots of samples (a): ○, HSM100-2; ◇, HSM150-2; □, HSM200-2; ◆, HSM150-4 and (b) △, SM2; ▲, SM4.

Table 5. Electrochemical performances recently reported for various biomass-based activated carbons

Biomass precursor	S_{BET} (m^2 g^{-1})	C (F g^{-1}) at 0.5 A g^{-1}	Energy density (Wh Kg^{-1}) / power density (kW kg^{-1})	Electrolyte	Reference
Sunflower stalk	1505	365	35.7 / 0.98	6M KOH	14
Mangosteen peel	965	270	n.d.	6M KOH	15
Rice husk	1897	250	n.d.	6M KOH	16
Bamboo shoot shells	3300	209	8.9 / 2.9	6M KOH	17
Melia Azedarach	1032	240	27.4 / 0.11	1M H_2SO_4	25
Rapeseed	682	250	13.5 / 0.4	6M KOH	43
Chinese fir sawdust	2294	225	7.8 / 0.25	6M KOH	44
Fir sawdust	2395	242	8.4 / 0.25	6M KOH	45
Pteroceltis tatarinowii	1210	206	n.d.	1M H_2SO_4	46
Banana skin	1200	130	n.d.	6M KOH	47
Enteromorpha prolifera	1528	200	9.5 / 0.4	6M KOH	48
Bamboo shoots	1309	223 at 1 A g^{-1}	13.1 / 0.54	1M H_2SO_4	49
Wheat straw	892	257	n.d.	6M KOH	50
Plane tree fruit fluff	1533	258 at 1 A g^{-1}	n.d.	6M KOH	51
Baobab fruit shells	1059	234 at 1 A g^{-1}	n.d.	6M KOH	52
Green tea wastes	1058	162	n.d.	1M H_2SO_4	53
Sawdust	1674	367	8.7 / 0.25	6M KOH	54
Schinus molle stones	627	235	7.8 / 0.4	1M H_2SO_4	This study

Figure 7 depicts the Ragone plots of the ACs, revealing the dependence between energy and power density. The maximum energy density increased with higher HTC temperature in the HSM series and decreased with a higher degree of activation in both series. These results were again attributed to variations in the surface functionality contents and porosity of the ACs. The energy density decreased at higher power density (Fig. 7), and the HSM200-2 sample showed the highest energy density 7.83 Wh kg^{-1} at a power density of 400 W kg^{-1}. The electrochemical performance of this sample was comparable to that recently reported for ACs from various biomass wastes (Table 5).

4. CONCLUSIONS

The ash content was lower and the N content higher in ACs produced by the HTC-KOH activation of SM stones than in ACs produced by the direct KOH activation of pristine SM stones. This difference is attributable to solubilization of the inorganic matter of the precursor and to Maillard-type reactions during the HTC process. Examination of the porosity and surface area of the ACs indicated that SM stones were more reactive to KOH activation after HTC. We highlight the very large surface area of HSM150-4, 1464 m^2 g^{-1}, with a mesopore volume of 0.29 cm^3 g^{-1} that represented *ca*. 32 % of the total porosity.

HSM200-2 showed the highest gravimetric capacitance, 235 F g^{-1}, at 0.5 A g^{-1}, and the highest energy density, 7.83 Wh kg^{-1}, at a power density of 400 W kg^{-1}. These values are comparable to those recently reported for ACs from various biomass wastes.

ACKNOWLEDGMENTS
This study was supported by the Junta de Andalucía (grant numbers P12-RNM-2892, RNM172). HGR gratefully acknowledges the support of COLCIENCIAS (Colombia) for her PhD studies.

References

1. M. Smisek and S. Cerny, Active carbon, manufacture, properties and applications, Elsevier: Amsterdam, The Netherlands, 1970
2. R.C. Bansal, J.B. Donnet and F. Stoeckli, Active Carbon, Marcel Dekker: New York, USA, 1988.
3. F. Rodríguez-Reinoso, Introduction to Carbon Technologies, University of Alicante: Alicante, Spain, 1997.
4. F. Derbyshire, M. Jagtoyen, R. Andrews, A.M. Rao, I. Martín-Gullón and E.A. Grulke, Chemistry and Physics of Carbon, Vol. 27, Ch. 1, Marcel Dekker: New York, USA, 2001.
5. L.R. Radovic, C. Moreno-Castilla and J. Rivera-Utrilla, Chemistry and Physics of Carbon, Vol. 27, Ch. 4, Marcel Dekker: New York, USA, 2001.
6. F. Béguin, V. Presser, A. Balducci and E. Frackowiak, *Adv. Mater*., 26 (2014) 2219.
7. A.M. Abioye and F.N. Ani, *Renew. Sust. Energ. Rev*., 52 (2015) 1282.
8. A. Jain, R. Balasubramanian and M.P. Srinivasan, *Chem. Eng. J*., 283 (2016) 789.
9. Q. Ma, Y. Yu, M. Sindoro, A.G. Fane, R. Wang and H. Zhang, *Adv. Mater*., 29 (2017) 1605361.
10. K. Mensah-Darkwa, C. Zequine, P.K. Kahol, and R.K. Gupta, *Sustainability*, 11 (2019) 414.

11. A. Linares-Solano, D. Lozano-Castelló, M.A. Lillo-Ródenas, D. Cazorla-Amorós, Chemistry and Physics of Carbon, Vol. 30, Ch. 1, CRC Press: New York, USA, 2008.
12. F. Quesada-Plata, R. Ruiz-Rosa, E. Morallón and D. Cazorla-Amorós, *ChemPlusChem,* 81 (2016) 1349.
13. E. Atta-Obeng, B. Dawson-Andoh, M.S. Seehra, U. Geddam, J. Poston and J. Leisen, *Biomass Bioener*., 107 (2017) 172.
14. X. Wang, S. Yun, W. Fang, C. Zhang, X. Liang, Z. Lei and Z. Liu, *ACS Sustain. Chem. Eng*., 6 (2018) 11397.
15. Y. Lia, X. Wanga and M. Cao, *J. CO_2 Util*., 27 (2018) 204.
16. C. Li, D. He, Z-H. Huang and M-X. Wang, *J. Electrochem. Soc.,* 165 (2018) A3334.
17. G. Huang, Y. Wang, T. Zhang, X. Wu and J. Cai, *J. Taiwan Inst. Chem. Eng*., 96 (2019) 672.
18. M.M. Titirici, R. White, C. Falco and M. Sevilla, *Energy Environ*. *Sci*., 5 (2012) 6796.
19. M.M. Titirici, A. Funke and A. Kruse, Recent Advances in Thermo-Chemical Conversion of Biomass, Ch. 12, Elsevier: Boston, USA, 2015.
20. N. Manyala, A. Bello, F. Barzegar, A.A. Khaleed, D.Y. Momodu and J.K. Dangbegnon, *Mater. Chem. Phys*., 182 (2016) 139.
21. A. Guerrero-Ruiz, I. Rodríguez-Ramos, F. Rodríguez-Reinoso, C. Moreno-Castilla and J. D. López-González, *Carbon*, 26 (1988) 417.
22. M. Wang, J. Fu, J. Zhu, Y. Yan and Q. Xu, *RSC Adv*., 5 (2015) 28080.
23. K.Y. Kang, B.I. Lee and J.S. Lee, *Carbon*, 47 (2009) 1171.
24. L. Zhao, L.Z. Fan, M.Q. Zhou, H. Guan, S. Qiao, M. Antonietti and M.M. Titirici, *Adv. Mater*., 22 (2010) 5202.
25. C. Moreno-Castilla, H. García-Rosero and F. Carrasco-Marín, *Materials*, 10 (2017) 747.
26. T.E. Rufford, D. Hulicova-Jurcakova, E. Fiset, Z. Zhu and G.Q. Lu, *Electrochem. Commun*., 11 (2009) 974.
27. G.A. Ferrero, A.B. Fuertes and M. Sevilla, *Electrochim. Acta*, 168 (2015) 320.
28. T. Liang, C. Chen and X. Li, J. Zhang, *Langmuir*, 32 (2016) 8042.
29. C.D. Wagner, X-Ray Photoelectron Spectroscopy Database. Version 1.0 NIST Standard Reference Database 20. National Institute of Standards and Technology: Gaithersburg, USA, 1989.
30. J.R. Pels, F. Kapteijn, J.A. Moulijn, Q. Zhu and K.M. Thomas, *Carbon*, 33 (1995) 1641.
31. M. Pérez-Cadenas, C. Moreno-Castilla, F. Carrasco-Marín and A. F. Pérez-Cadenas, *Langmuir*, 25 (2009) 466.
32. D. Wang, M. Chen, C. Wang, J. Bai and J. Zheng, *Mater. Lett*., 65 (2011) 1069.
33. M. Seredych, D. Hulicova-Jurcakova, G.Q. Lu and T.J. Bandosz, *Carbon*, 46 (2008) 1475.
34. Z.W. He, J. Yang, Q.F. Lü and Q. Lin, *ACS Sustain. Chem. Eng*., 1 (2013) 334.
35. M. Thommes, K. Kaneko, A.V. Neimark, J.P. Olivier, F. Rodríguez-Reinoso, J. Rouquerol and K.S.W. Sing, *Pure Appl. Chem*., 87 (2015) 1051.
36. F. Rodríguez-Reinoso and A. Linares-Solano, Chemistry and Physics of Carbon, Vol. 21, Ch. 1, Marcel Dekker: New York, USA, 1989.
37. D. Cazorla-Amorós, J. Alcañiz-Monge, M.A. De la Casa-Lillo and A. Linares-Solano, *Langmuir*, 14 (1998) 4589.
38. M.D. Stoller and R.S. Ruoff, *Energy Environ. Sci*., 3 (2010) 1294.
39. E. Raymundo-Piñero and F. Béguin, Activated Carbon Surfaces in Environmental Remediation, Elsevier: Oxford,UK, 2006.
40. G.A. Ferrero, A.B. Fuertes and M. Sevilla, *Sci. Rep*., 5 (2015) 16618.
41. D. Hulicova, M. Kodama and H. Hatori, *Chem. Mater*., 18 (2006) 2318.
42. C. Moreno-Castilla, M.B. Dawidziuk, F. Carrasco-Marín and E. Morallón, *Carbon*, 50 (2012) 3324.
43. K. Sun and D. Guo, *Int. J. Electrochem. Sci*., 11 (2016) 4743.
44. Y. Huang, L. Peng, Y. Liu, G. Zhao, J.Y. Chen and G. Yu, *ACS Appl. Mater. Inter*., 8 (2016) 15205.

45. Y. Huang, Y. Liu, G. Zhao and J.Y. Chen, *J. Mater. Sci*., 52 (2017) 478.
46. Z. Sun, J. Liao, B. Sun, M. He, X. Pan, J. Zhu, C. Shi and Y. Jiang, *Int. J. Electrochem. Sci*., 12 (2017) 12084.
47. K. Wasiński, P. Nowicki, P. Półrolniczak, M. Walkowiak and R. Pietrzak, *Int. J. Electrochem. Sci*., 12 (2017) 128.
48. M. Ren, Z. Jia, Z. Tian, D. López, J. Cai, M.M. Titirici and A.B. Jorge, *ChemElectroChem*, 5 (2018) 2686.
49. J. Han, Q. Li, J. Wang, J. Ye, G. Fu, L. Zhai and Y. Zhu, *J. Mater. Sci-Mater. El*., 29 (2018) 20991.
50. W. Liu, J. Mei, G. Liu, Q. Kou, T. Yi and S. Xiao, *ACS Sustain. Chem. Eng*., 6 (2018) 11595.
51. D. He, Z‐H. Huang and M‐X. Wang, *J. Mater. Sci-Mater. El*., 30 (2019) 1468.
52. A.A. Mohammed, C. Chen and Z. Zhu, *J. Colloid Interface Sci*., 538 (2019) 308.
53. S. Sankar , A.T.A. Ahmed , A.I. Inamdar, H. Im, Y.B. Im, Y. Lee, D.Y. Kim and S. Lee, *Mater. Des*., 169 (2019) 107688.
54. D. Guo, R. Xin, Y. Wang, W. Jiang, Q. Gao, G. Hu and M. Fan, *Microp. Mesop. Mater.,* 279 (2019) 323.